

# Terahertz quantum illumination using free-electron lasers

Linfeng Zhang,<sup>1</sup> Leshi Zhao,<sup>1</sup> Haitan Xu<sup>1,2,3,4,\*</sup> and Zheng Li<sup>1,5,6,†</sup>

<sup>1</sup>*State Key Laboratory for Mesoscopic Physics and Collaborative Innovation Center of Quantum Matter, School of Physics, Peking University, Beijing 100871, China*

<sup>2</sup>*School of Materials Science and Intelligent Engineering, Nanjing University, Suzhou, Jiangsu 215163, China*

<sup>3</sup>*Shishan Laboratory, Nanjing University, Suzhou, Jiangsu 215163, China*

<sup>4</sup>*School of Physical Sciences, University of Science and Technology of China, Hefei, Anhui 230026, China*

<sup>5</sup>*Collaborative Innovation Center of Extreme Optics, Shanxi University, Taiyuan, Shanxi 030006, China*

<sup>6</sup>*Peking University Yangtze Delta Institute of Optoelectronics, Nantong, Jiangsu 226010, China*



(Received 10 November 2023; revised 2 January 2024; accepted 16 May 2024; published 10 June 2024)

We propose a terahertz quantum illumination (QI) scheme utilizing emissions from free-electron lasers (FELs) based on joint photon number measurement and quantum state discrimination using maximum *a posteriori* estimation. We analyze the performance of our QI scheme and quantify it with error probabilities. We numerically demonstrate the quantum advantage of our QI scheme over classical illumination. Our work paves the way to using FELs as entangled photon sources for quantum illumination in the terahertz regime.

DOI: 10.1103/PhysRevApplied.21.064021

## I. INTRODUCTION

The terahertz (THz) frequency regime (0.1–10 THz) of the electromagnetic spectrum draws growing interest in various areas from both scientific and technological perspectives. The past decade has witnessed progress in this area with the development of terahertz imaging [1–3] and radar technologies [4–6] for its noninvasive inspection of semiconductors and biological tissues as well as its improved resolving power and larger bandwidth over microwave frequencies. Yet, deployment of such technologies demands high-performance terahertz sources [7–10] and detectors [11–14].

Meanwhile, quantum illumination (QI) by nonclassical light can provide better performance than classical light when detecting and imaging objects in the presence of high levels of noise and loss [15]. QI has been studied theoretically in optical [16–18] and microwave [19,20] frequencies, and experimentally demonstrated in optical frequencies for different entangled degrees of freedom [21–23]. However, quantum illumination with terahertz photons has not been investigated to date.

Here we propose a terahertz quantum illumination scheme with a free-electron laser (FEL) as a nonclassical light source. We showcase that the FEL can efficiently generate entangled photon pairs of terahertz frequency, the

states of which are approximately Bell states in the polarization degree of freedom. Then we elaborate on the QI scheme, which is based on joint photon number measurements and a quantum state discrimination strategy, and analyze its performance quantified by error probabilities. We numerically demonstrate the quantum advantage of our QI scheme over classical illumination with the same light intensity.

## II. ENTANGLED TERAHERTZ EMISSION FROM FEL

In Fig. 1 we sketch the terahertz QI scheme with entangled emission from a FEL. Figure 1(a) shows the FEL process in the laboratory frame. A relativistic electron bunch travels through an undulator and interacts with the magnetic field inside, resulting in electron microbunching and amplified emission.

To facilitate the characterization of the emission from the FEL, we shift to the electron frame (EF), where the incident electron bunch has a zero mean initial velocity. Using the Weizsäcker-Williams theory [24], the emission from the FEL can be approximated as the scattering of the undulator-transformed quasielectromagnetic wave from the electron bunch in the EF, which can be calculated with quantum electrodynamics theory, as demonstrated in our previous work [25]. Double emissions entangled in both energy and polarization can be generated in certain directions.

\*Corresponding author: haitanxu@nju.edu.cn

†Corresponding author: zheng.li@pku.edu.cn

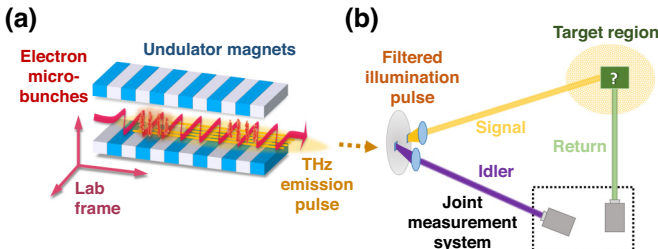


FIG. 1. Schematic of terahertz quantum illumination by entangled emission from a FEL. (a) Illustration of entangled emission from a FEL in the laboratory frame. In such a frame, premicrobunched electrons are injected into an undulator and generate terahertz emission via wiggling motion. The resulting emission has nonlinear components dominated by double emission. (b) Schematic of a terahertz quantum illumination system. After filtering, the two-mode emission from the FEL is directed to the QI system. Photons in one beam act as the probe to illuminate the target region, while photons in the other beam are sent to the detector as ancilla. By a joint measurement we can determine whether an object is present in the target region.

With the FEL parameters in Table I, we numerically simulate the entangled terahertz emission with  $\omega_1 \simeq \omega_{\text{fd}}/3 = 2\pi \times 0.566 \text{ THz}$  and  $\omega_2 \simeq 5\omega_{\text{fd}}/3 = 2\pi \times 2.83 \text{ THz}$ , and the configuration of the system is shown in Fig. 2(a). The differential emission rate and the concurrence of the double emission for various angular configurations are illustrated in Figs. 2(b) and 2(c), respectively. Certain angular configurations can result in emitted photon pairs approximately in Bell states. The density matrix  $\hat{\rho}_f$  of the emitted photon pair for the configuration represented by the green and yellow dots in Figs. 2(b) and 2(c) is shown in Fig. 2(d).

### III. THEORY OF TERAHERTZ QUANTUM ILLUMINATION USING FEL

The main goal of QI is to determine whether a reflective object exists in a target region that has a bright noise bath as background [27]. In classical illumination, photons with density matrix of  $\hat{\rho}_{\text{cl}}$  are used to probe the target region. If the object is absent, the observed signal contains only the background with density matrix of  $\hat{\rho}_b$ , and thus the observed density matrix  $\hat{\rho}_{\text{cl}}^{(0)} = \hat{\rho}_b$ . If the target exists, the observed density matrix has a form of  $\hat{\rho}_{\text{cl}}^{(1)} = \kappa \hat{\rho}_{\text{cl}} + (1 - \kappa) \hat{\rho}_b$ , where the superscript 0, 1 labels

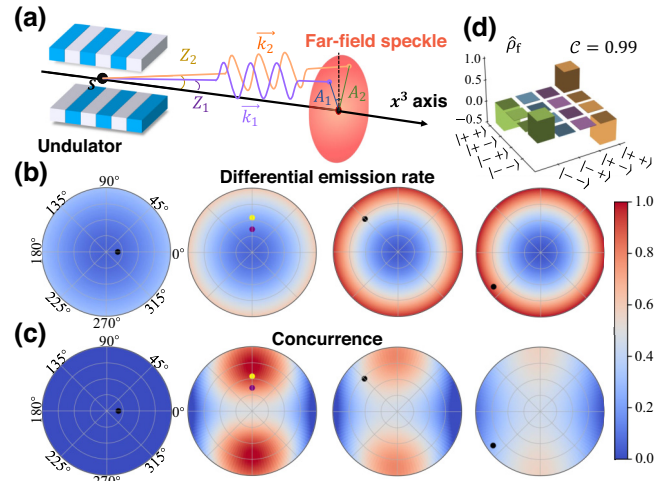


FIG. 2. Entangled emission from the FEL. (a) Illustration of the angular configuration parameters in (b),(c).  $Z_{1,2}$  and  $A_{1,2}$  are the zenith angles and the azimuth angles of the three-momentum  $\mathbf{k}_1, \mathbf{k}_2$  of the emitted photons, which are defined with respect to the point  $S$  at the center of undulator for far-field measurement. (b) Normalized double angular distribution of the differential scattering rate  $\frac{dW}{dk_1^0 d\Omega_1 d\Omega_2}$  in the laboratory frame by numerical simulation, where  $k_1^0 = \omega_1$  is the energy of photon 1 and  $\Omega_1$  and  $\Omega_2$  are the solid angles of the emitted photon pair. (c) Double angular distribution of the concurrence  $\mathcal{C}$  by numerical simulation. In (b),(c), the polar angle and the radii refer to  $A_2 \in [0, 2\pi]$  and  $\gamma \tan(Z_2) \in [0, 1]$  for photon 2, where  $\gamma$  is the Lorentz factor of the incident electrons. The black and purple dots represent different angular configurations of photon 1 for each plot. We choose  $\omega_1 \simeq \omega_{\text{fd}}/3$  and  $\omega_2 \simeq 5\omega_{\text{fd}}/3$ . (d) Reduced density matrix  $\hat{\rho}_f$  for the chosen angular configuration of the photon pair with  $\gamma \tan(Z_1) = 0.36$ ,  $\gamma \tan(Z_2) = 0.55$ ,  $A_1 = 90^\circ = A_2$ , where the concurrence  $\mathcal{C} = 0.99$  indicates nearly optimal entanglement, and the scattering rate is relatively high. In (b),(c), this angular configuration is marked with the purple point representing photon 1 and the yellow point representing photon 2. The density matrix corresponds to a Bell state approximately, which is useful for QI.

the absence and presence of the object, respectively, and  $\kappa$  contains information about reflection and propagation of the probe photon. With a series of repeated measurements, a discrimination between two quantum state candidates  $\hat{\rho}_{\text{cl}}^{(0)}$  and  $\hat{\rho}_{\text{cl}}^{(1)}$  is performed to determine whether the object is present or not in the target region.

TABLE I. The free-electron laser parameters for numerical simulation in this work, based on the terahertz beamline of FLASH FEL [26].

Electron energy	0.5 GeV	Number of periods	20
Charge per bunch	0.50 pC	Fundamental wavelength	177 μm
Repetition rate	5.0 kHz	RMS bunch length	10 μm
Undulator field	1.1 T	Emission pulse FWHM	approximately 1 ps
Undulator period	40 cm		

In quantum illumination, nonclassical light is utilized to better observe the object in the target region. We use photons from signal and idler modes with joint density matrix of  $\hat{\rho}_{\text{qu}}$ . Photons of the signal mode are sent to probe the target region, while those in the idler mode are directly sent to the detector. We make joint measurement on the return mode from the target region and the idler mode. When the object is absent, the photons collected from the target region are purely from the background, and thus the observed density matrix is  $\hat{\rho}_{\text{qu}}^{(0)} = \hat{\rho}_b \otimes \text{Tr}_S[\hat{\rho}_{\text{qu}}]$ , where  $\text{Tr}_S$  is the partial trace over the signal mode. When the object is present, the observed density matrix has a form of  $\hat{\rho}_{\text{qu}}^{(1)} = \kappa \hat{\rho}_{\text{qu}} + (1 - \kappa) \hat{\rho}_b \otimes \text{Tr}_S[\hat{\rho}_{\text{qu}}]$ . Here the presence of the object can be determined from the discrimination between  $\hat{\rho}_{\text{qu}}^{(0)}$  and  $\hat{\rho}_{\text{qu}}^{(1)}$ . For joint detection of terahertz photons, we also need to consider the background noise in the idler mode.

Now we consider the density matrix of the FEL-emitted photons in Fock basis, i.e.,  $\hat{\rho}_{\text{qu}} = \hat{\rho}_{\text{FEL}}^{\text{Fock}}$ . The diagonal components of the density matrix  $\hat{\rho}_{\text{FEL}}^{\text{Fock}}$  can be denoted as  $N_0|0_S 0_I\rangle\langle 0_S 0_I|$ ,  $N_S|1_S 0_I\rangle\langle 1_S 0_I|$ ,  $N_I|0_S 1_I\rangle\langle 0_S 1_I|$ , and  $N_C|1_S 1_I\rangle\langle 1_S 1_I|$ , where  $0 < N_C, N_S, N_I \ll N_0 < 1$  can be calculated from the scattering theory and satisfy  $N_C + N_S + N_I + N_0 \simeq 1$ .

Then we introduce thermal noises on both the return mode and the idler mode with the form of  $\hat{\rho}^{\text{th}}(\bar{N}_b) = \sum_{j=0}^{+\infty} w_b(j)|j\rangle\langle j|$ , where  $w_b(j) = [\bar{N}_b^j / (\bar{N}_b + 1)^{j+1}]$ , and the average photon number  $\bar{N}_b = \bar{N}_{bR}$  for the return mode and  $\bar{N}_b = \bar{N}_{bI}$  for the idler mode. The density matrices are  $\hat{\rho}_{bS} = \hat{\rho}^{\text{th}}(\bar{N}_{bS})$  and  $\hat{\rho}_{bI} = \hat{\rho}^{\text{th}}(\bar{N}_{bI})$  for single-mode thermal states. Similar to  $\kappa$  for the return mode, we use another mixed ratio  $\zeta$  to reflect the weight of the quantum signal relative to the background noise in the idler mode. The density matrix with the background on both modes is obtained as

$$\begin{aligned}\hat{\rho}_{\text{qu}}^{(0)} &= \zeta \hat{\rho}_{bS} \otimes \text{Tr}_S[\hat{\rho}_{\text{qu}}] + (1 - \zeta) \hat{\rho}_{bS} \otimes \hat{\rho}_{bI}, \\ \hat{\rho}_{\text{qu}}^{(1)} &= \kappa \left\{ \zeta \hat{\rho}_{\text{qu}} + (1 - \zeta) \text{Tr}_I[\hat{\rho}_{\text{qu}}] \otimes \hat{\rho}_{bI} \right\} + (1 - \kappa) \hat{\rho}_{\text{qu}}^{(0)}.\end{aligned}\quad (1)$$

Accordingly, we can obtain the diagonal elements  $d_{mn}^{(0)} = \rho_{\text{qu},mn,mn}^{(0)}$  and  $d_{mn}^{(1)} = \rho_{\text{qu},mn,mn}^{(1)}$  of the two density matrices  $\hat{\rho}_{\text{qu}}^{(0)}$  and  $\hat{\rho}_{\text{qu}}^{(1)}$  to be discriminated in QI as follows:

$$\begin{aligned}d_{mn}^{(0)} &= w_{bR}(m)[\zeta \delta_{n0}(N_0 + N_S) + \zeta \delta_{n1}(N_I + N_C) \\ &\quad + (1 - \zeta)w_{bI}(n)]\end{aligned}\quad (2)$$

and

$$\begin{aligned}d_{mn}^{(1)} &= \kappa \{ \zeta (\delta_{m0}\delta_{n0}N_0 + \delta_{m1}\delta_{n0}N_S + \delta_{m0}\delta_{n1}N_I \\ &\quad + \delta_{m1}\delta_{n1}N_C) + (1 - \zeta) [\delta_{m0}(N_0 + N_I) \\ &\quad + \delta_{m1}(N_S + N_C)]w_{bI}(n) \} + (1 - \kappa)d_{mn}^{(0)},\end{aligned}\quad (3)$$

respectively, where  $m, n = 0, 1, 2, \dots$  refer to the photon numbers on the return and idler modes.

We now consider a direct joint photon number measurement scheme of QI, as shown in Fig. 1(b). Via spatial and spectral filtering, we acquire two modes of the emission from the FEL that contains the double emission component for QI application. Each emission pulse is used as an illumination pulse.

For practical instruments, the timescales satisfy  $t_{\text{rep}} \gg t_{\text{res}} \gg t_{\text{pul}}$ , where  $t_{\text{rep}}$  refers to the time interval between adjacent illumination pulses,  $t_{\text{res}}$  refers to the time resolution of the THz photodetectors, and  $t_{\text{pul}}$  refers to the duration of the illumination pulse. Thus, the joint measurement system with two THz photodetectors can determine whether photons in the return and idler modes are from the same illumination pulse, but without detailed resolution within each pulse. Even with such a limited practical measurement of photon numbers in the return and idler modes, we can still determine the presence of the target with enhanced accuracy.

We propose a discrimination procedure based on the principle of maximum *a posteriori* estimation (MAPE) [28], which is schematically demonstrated in Fig. 3. There are four different outcome combinations from the joint measurement of the return and idler modes, i.e., no photons are received by either photodetector, photons from the idler and return modes are received by both photodetectors, only photons in the return mode are received by the corresponding photodetector, and only photons from the idler mode are received by the corresponding photodetector. We label such outcome combinations with O, C, R, and I, respectively. As shown in Fig. 3(a), for a joint measurement with  $M$  illumination pulses, we can obtain the corresponding count numbers for each outcome combination, denoted by an ordinal array  $\langle M_O, M_R, M_I, M_C \rangle$ .

When the object is absent in the target region, denoted by the superscript (0), the probabilities of observing O, R, I and C are related to the diagonal elements of the observed density matrix  $\hat{\rho}_{\text{qu}}^{(0)}$  in Eq. (2) via  $d_O^{(0)} = d_{00}^{(0)}$ ,  $d_R^{(0)} = \sum_{m=1}^{+\infty} d_{m0}^{(0)}$ ,  $d_I^{(0)} = \sum_{n=1}^{+\infty} d_{0n}^{(0)}$ ,  $d_C^{(0)} = \sum_{m,n=1}^{+\infty} d_{mn}^{(0)}$ . When the object is present in the target region, denoted by the superscript (1), the probabilities of observing O, R, I and C are related to the diagonal elements of the observed density matrix  $\hat{\rho}_{\text{qu}}^{(1)}$  in Eq. (3) via  $d_O^{(1)} = d_{00}^{(1)}$ ,  $d_R^{(1)} = \sum_{m=1}^{+\infty} d_{m0}^{(1)}$ ,  $d_I^{(1)} = \sum_{n=1}^{+\infty} d_{0n}^{(1)}$ ,  $d_C^{(1)} = \sum_{m,n=1}^{+\infty} d_{mn}^{(1)}$ . Also, the property of density matrices guarantees that  $d_O^{(j)} + d_R^{(j)} + d_I^{(j)} + d_C^{(j)} = 1$ . For the case  $j = 0, 1$ , with  $M$  illumination pulses we will obtain the ordinal array  $\langle M_O, M_R, M_I, M_C \rangle$  as a 4-tuple random vector that obeys a multinomial distribution with a joint probability mass function of

$$\begin{aligned}P(\langle M_O, M_R, M_I, M_C \rangle | j) &= C_{\text{Mn}}(M_O, M_R, M_I, M_C) (d_O^{(j)})^{M_O} \\ &\quad \times (d_R^{(j)})^{M_R} (d_I^{(j)})^{M_I} (d_C^{(j)})^{M_C}\end{aligned}\quad (4)$$

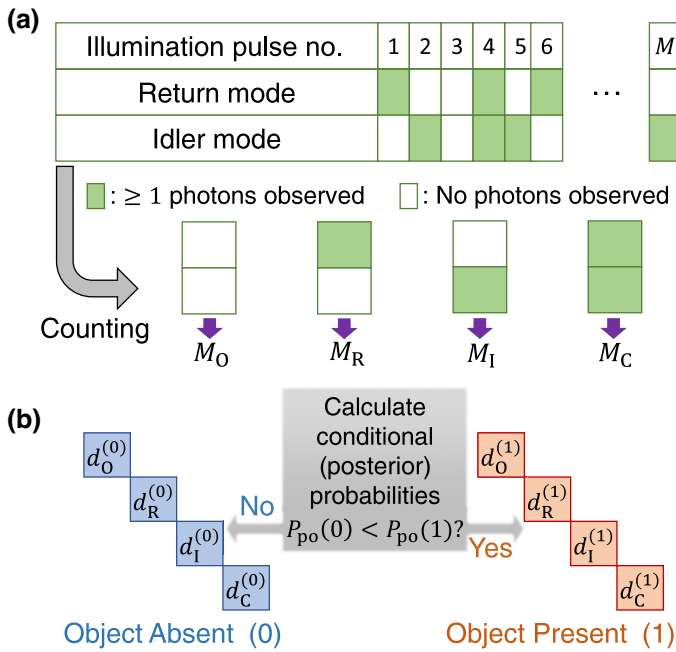


FIG. 3. Discrimination procedure of the QI scheme based on direct joint photon number measurement. (a) Joint photon measurement process. For each illumination pulse, we use THz photodetectors to record the photons from the return and idler modes. The filled and open rectangles refer to the cases that at least one photon is observed and that no photon is observed, respectively. With the outcomes from both photodetectors for each illumination pulse, we can obtain the total count numbers  $M_O$ ,  $M_R$ ,  $M_I$ , and  $M_C$  for different outcome combinations of the joint measurement, and  $M = M_O + M_R + M_I + M_C$  is the total number of illumination pulses. Here the subscript O denotes the outcome combination that no photons are received by either photodetector, subscript C denotes the outcome combination that photons from the return and idler modes are received by both photodetectors, subscript R denotes the outcome combination that only photons in the return mode are received by the corresponding photodetector, and subscript I denotes the outcome combination that only photons from the idler mode are received by the corresponding photodetector. (b) Determination of the presence of the object based on the principle of MAPE with the count numbers  $M_O$ ,  $M_R$ ,  $M_I$ ,  $M_C$ . Specifically, for a certain prior distribution, we can calculate the conditional or posterior probabilities  $P_{po}(0) = P(0|\langle M_O, M_R, M_I, M_C \rangle)$  and  $P_{po}(1) = P(1|\langle M_O, M_R, M_I, M_C \rangle)$  via the Bayesian theorem. If  $P_{po}(0) < P_{po}(1)$ , we decide that there is an object in the target region, otherwise the object is absent.

for any  $\langle M_O, M_R, M_I, M_C \rangle$  with all elements being non-negative integers that satisfy  $M_O + M_R + M_I + M_C = M$  and otherwise  $P(\langle M_O, M_R, M_I, M_C \rangle | j) = 0$ . Here  $C_{Mn}(M_O, M_R, M_I, M_C) = \Gamma(M)/[\Gamma(M_O)\Gamma(M_R)\Gamma(M_I)\Gamma(M_C)]$  is the multinomial coefficient and  $\Gamma$  is the gamma function.

Based on the knowledge above and a prior distribution  $\{P_{pr}(0), P_{pr}(1)\}$ , we can calculate the conditional probabilities  $P(0|\langle M_O, M_R, M_I, M_C \rangle)$  and  $P(1|\langle M_O, M_R, M_I, M_C \rangle)$

via the Bayesian theorem:

$$\begin{aligned} P(j|\langle M_O, M_R, M_I, M_C \rangle) &= \frac{P(\langle M_O, M_R, M_I, M_C \rangle | j) P_{pr}(j)}{P(\langle M_O, M_R, M_I, M_C \rangle)} \\ &= \frac{P_{pr}(j) F_j}{P_{pr}(0) F_0 + P_{pr}(1) F_1}, \end{aligned} \quad (5)$$

where  $P(\langle M_O, M_R, M_I, M_C \rangle) = P(\langle M_O, M_R, M_I, M_C \rangle | 0) P_{pr}(0) + P(\langle M_O, M_R, M_I, M_C \rangle | 1) P_{pr}(1)$  and  $F_j = (d_O^{(j)})^{M_O} (d_R^{(j)})^{M_R} \times (d_I^{(j)})^{M_I} (d_C^{(j)})^{M_C}$  for  $j = 0, 1$ . In Bayesian theory, one calls such conditional probabilities as posterior probabilities  $P_{po}(j) = P(j|\langle M_O, M_R, M_I, M_C \rangle)$ . We make a judgement based on the posterior probabilities  $P_{po}(j)$ . If  $P_{po}(0) < P_{po}(1)$ , we decide that there is an object in the target region. Otherwise, we decide that the object is absent in the target region. Such a judgement procedure is in essence a maximum *a posteriori* estimation.

For any specific array of count numbers  $\langle M_O, M_R, M_I, M_C \rangle$  with  $M$  illumination pulses, we obtain the posterior probabilities  $P_{po}(j)$  with  $j = 0, 1$ . We can further evaluate the performance of the MAPE procedure by the error probability  $P_{err}^{MAPE}(M)$  defined as

$$\begin{aligned} P_{err}^{MAPE}(M) &= \sum_{\langle M_O, M_R, M_I, M_C \rangle} P(\langle M_O, M_R, M_I, M_C \rangle) \\ &\quad \times \inf(\{P_{po}(0), P_{po}(1)\}) \\ &= \sum_{\langle M_O, M_R, M_I, M_C \rangle} C_{Mn}(M_O, M_R, M_I, M_C) \\ &\quad \times \inf(\{P_{pr}(0) F_0, P_{pr}(1) F_1\}), \end{aligned} \quad (6)$$

where  $\inf()$  refers to the infimum of the given set.

For comparison, we also consider the classical illumination scheme using a coherent state with the same average number  $N_A$  of probe photons as the signal mode, i.e.,  $N_A = N_S + N_C$ . The error probability of the classical illumination scheme satisfies  $P_{err,cl}(M) \leq \exp(-M\kappa N_A/4\bar{N}_{bR})/2$  and  $P_{err,cl}(M) \geq [1 - \sqrt{1 - \exp(-M\kappa N_A/2\bar{N}_{bR})}]/2$  [16,29].

#### IV. NUMERICAL SIMULATION OF TERAHERTZ QUANTUM ILLUMINATION USING FEL

We now carry out a numerical simulation of THz QI. The parameters of the FEL are shown in Table I, and the proposed THz photon detection can be implemented with quantum capacitance detectors at THz frequency [13].

By numerically calculating the emission rates of the signal and idler modes, we can obtain  $N_C$ ,  $N_S$ ,  $N_I$ ,  $N_0$  in Eqs. (2) and (3) as

$$\begin{aligned}
N_C &= N_D + (\Sigma_S - N_D)(\Sigma_I - N_D), \\
N_S &= (\Sigma_S - N_D)(1 - \Sigma_I), \\
N_I &= (\Sigma_I - N_D)(1 - \Sigma_S), \\
N_0 &= 1 - N_C - N_S - N_I,
\end{aligned} \tag{7}$$

where

$$\begin{aligned}
N_D &= F_{mb} t_{pass} \int_{\Delta\Omega_1} d\Omega_1 \int_{\Delta\Omega_2} d\Omega_2 \int_{\omega_1^-}^{\omega_1^+} dk_1^0 \frac{d\dot{W}}{dk_1^0 d\Omega_1 d\Omega_2} (n = 2), \\
\Sigma_S &= F_{mb} t_{pass} \left\{ \int d\Omega_1 \int_{\Delta\Omega_2} d\Omega_2 \int_{\omega_2^-}^{\omega_2^+} dk_2^0 \sum_n \frac{d\dot{W}}{dk_2^0 d\Omega_1 d\Omega_2} (n) + F_s(\omega_2) \int_{\Delta\Omega_2} d\Omega_2 \int_{\omega_2^-}^{\omega_2^+} dk_2^0 \frac{d\dot{W}}{dk_2^0 d\Omega_2} \right\}, \\
\Sigma_I &= F_{mb} t_{pass} \left\{ \int_{\Delta\Omega_1} d\Omega_1 \int d\Omega_2 \int_{\omega_1^-}^{\omega_1^+} dk_1^0 \sum_n \frac{d\dot{W}}{dk_1^0 d\Omega_1 d\Omega_2} (n) + F_s(\omega_1) \int_{\Delta\Omega_1} d\Omega_1 \int_{\omega_1^-}^{\omega_1^+} dk_1^0 \frac{d\dot{W}}{dk_1^0 d\Omega_1} \right\}.
\end{aligned} \tag{8}$$

In Eq. (8),  $F_{mb}$  refers to the microbunching enhancement factor, which depends only on the electron distribution, and  $t_{pass}$  refers to the time for the electron bunch to pass through the undulator. We calculate the differential double emission rates such as  $\frac{d\dot{W}}{dk_2^0 d\Omega_1 d\Omega_2}(n)$  via the techniques in our previous work [25], and the differential single emission rates such as  $\frac{d\dot{W}}{dk_1^0 d\Omega_1}$  as in Ref. [30]. The frequency-relevant factor  $F_s(\omega)$  reflects the spectral broadening of the single emission, which depends on the shape of the undulator field.

The incident electron bunch with a charge of 0.50 pC (referring to electron amount of  $N_e \simeq 3.12 \times 10^6$ ) is accelerated to an average energy of 0.5 GeV (referring to  $\gamma \simeq 978.5$ ). The undulator provides a linearly polarized magnetic field with an amplitude of 1.1 T and a spatial period of 40 cm. The corresponding undulator parameter is  $K \simeq 41.1$  [31], and  $t_{pass} \simeq 26.7$  ns. Then we obtain the fundamental emission wavelength of 177 μm (referring to the frequency of 1.70 THz), the Pierce parameter of approximately 0.062, and the coherent length of the electrons about 129 μm [31]. As the electron bunch length is about 10 μm, which is much smaller than the coherent length, there exists only one microbunch, leading to a nearly fully coherent emission, i.e.,  $F_{mb} = N_e^2$ . The emission pulse duration is  $t_{pul} \sim t_{pass}/\gamma \sim 27$  ps, while the resolution time of the coincidence system of the quantum capacitance detectors is  $t_{res} \sim 1$  ns, and the average time interval between adjacent emission pulses is  $t_{rep} = 1/5.0$  kHz = 200 μs. Thus the condition  $t_{rep} \gg t_{res} \gg t_{pul}$  is satisfied, and we can tell whether the photons in the return and idler modes are from the same illumination pulse.

To select the entangled photons, we can place a spatial filter at the far-field region, e.g., 80 m from the undulator,

which is 10 times the undulator length. The filter has two holes with areas of about 58 and 87 mm<sup>2</sup>, corresponding to solid angles of  $\pi/363\gamma^2$  and  $\pi/242\gamma^2$ , respectively. The first hole is centered at  $\gamma\tan Z = 0.36$ ,  $A = \pi/2$  for photon 1 of the idler mode, while the second hole is centered at  $\gamma\tan Z = 0.55$ ,  $A = \pi/2$  for photon 2 of the signal mode. The entangled component of the filtered emission is shown in Fig. 2.

To make sure only the photons with energies around the chosen values are detected, an energy-filtering device at the THz range can be added in front of the photodetectors [13]. We choose the signal mode energy around  $\omega_S = \omega_2 = 5\omega_{fd}/3 \simeq 2\pi \times 2.83$  THz and the idler mode energy around  $\omega_I = \omega_1 = \omega_{fd}/3 \simeq 2\pi \times 0.566$  THz, both with energy ranges of [92%, 108%] relative to the chosen energies, due to the finite size of the holes of the spatial filter.

To estimate the factor  $F_s(\omega)$  in Eq. (8), we first consider an undulator with a rectangular profile bearing a sinusoidal magnetic field with constant amplitude inside a region with a transverse scale of approximately 1 mm and a longitudinal scale of 8 m. The resulting energy spectrum is of a  $\text{sinc}^2$  profile, and we can numerically obtain the component within the energy ranges of the signal and idler modes, which is approximately  $8.1 \times 10^{-4}$  relative to the total single emission rate. Then we consider a tapered undulator towards a polynomial approximation of the optimal Gaussian profile and obtain  $F_s(\omega_1) \sim F_s(\omega_2) \sim 10^{-4}$  for 20 periods. Thus, the contribution from the single emission is of a similar order of magnitude to that of the double emission in this case.

An emittance of the electron bunch of  $\gamma\epsilon \sim 1$  mm mrad and a relative energy spread of  $10^{-3}$  of the electrons result in minor effects on the emission rate and the entanglement degree. The emittance of  $\gamma\epsilon \sim 1$  mm mrad leads to

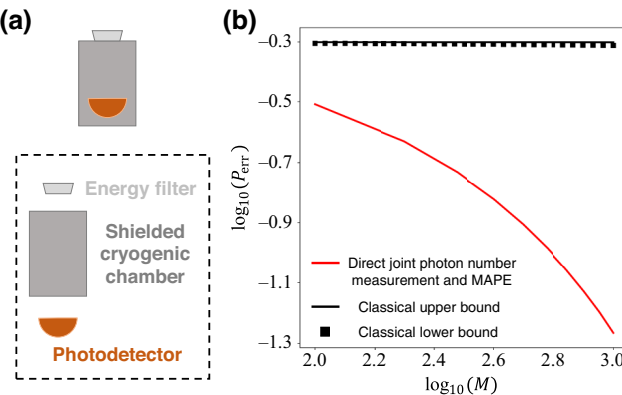


FIG. 4. Error probability of the QI scheme compared with that of the classical illumination scheme. (a) Schematic of the detectors used in the QI scheme as shown in Fig. 1, based on the quantum capacitance detector [13]. A shielded cryogenic chamber is used to suppress the thermal noise for the THz photodetector. (b) Numerical results of the error probabilities of different illumination schemes. The error probability of the QI scheme with direct joint photon number measurement and MAPE is significantly lower than that of the classical illumination scheme. The parameters used in the numerical calculations are  $\bar{N}_{\text{bR}} = 200$ ,  $\bar{N}_{\text{bI}} = 0.01$ ,  $N_S = 0.018$ ,  $N_I = 0.059$ ,  $N_C = 0.005$ ,  $\kappa = 0.01$ ,  $\zeta = 0.5$ .

an average beam size of about  $10^{-4}$  m and a momentum angular variance of about  $10^{-6}$  rad. These effects result in a variance of the emission rate of order  $10^{-3}$  and a spectral broadening of order  $10^{-3}$  according to numerical calculations, which are much smaller than that caused by the finite size of the holes of the spatial filter, and can be neglected in the numerical calculations.

For each illumination pulse, we obtain from Eqs. (7) and (8) that  $N_D \simeq 0.0039$ ,  $\Sigma_S \simeq 0.019$ ,  $\Sigma_I \simeq 0.060$ , and thus  $N_S \simeq 0.018$ ,  $N_I \simeq 0.059$ ,  $N_C \simeq 0.0050$  for such a single test. For numerical demonstration, we consider the background noises of  $\bar{N}_{\text{bR}} = 200$  and  $\bar{N}_{\text{bI}} = 0.01$  for the return and idler modes as an example. The background noise in the return mode is assumed to come from a bright bath in the target region [16]. The background noise in the idler mode is much smaller, as we assume that there is no bright bath in the idler path. We choose  $\kappa = 0.01$  if the object to be observed is assumed to have very low reflectivity [16] and  $\zeta = 0.5$  if the idler emission and the background noise in the idler path are of equal weight for the detector. With these given parameters, we can numerically calculate the error probability of the THz QI scheme with direct joint photon number measurement and MAPE using Eqs. (4)–(6) of the MAPE procedure, and compare it with that of the classical illumination scheme, as shown in Fig. 4. We can see from the numerical results the advantage of the QI scheme over classical illumination, which also applies to other choices of the parameters used in the numerical demonstration. Such quantum advantage comes from the existence of the entangled double emission component,

which contains correlated photon pairs on the two selected modes and makes the two quantum state candidates corresponding to the presence and the absence of the target more distinguishable.

## V. CONCLUSIONS

We present a proposal of a terahertz quantum illumination scheme with a free-electron laser, and theoretically analyze the terahertz QI scheme with joint photon number measurements and a discrimination procedure based on maximum *a posteriori* estimation. We numerically demonstrate the advantage of the quantum illumination scheme over classical illumination. With the terahertz QI scheme, we can combine the strengths of the terahertz radiation of large penetration depth and high resolution with the enhanced accuracy from the quantum advantage, which can have potential applications in future quantum imaging and detection technologies, especially for the circumstances where detection light with extremely weak intensity is needed.

## ACKNOWLEDGMENTS

The authors thank Zunqi Li, Mingsheng Tian, Chengyin Wu, and Qiongyi He for helpful discussions. This work was supported by the National Natural Science Foundation of China (Grants No. 12174009, No. 92250303, No. 12234002, No. 11974031, No. 12174011), Innovation Program for Quantum Science and Technology (Grant No. 2021ZD0301702), the National Key R&D Program of China (Grant No. 2023YFA1406801), the Natural Science Foundation of Jiangsu Province (Grant No. BK20232002), and Beijing Natural Science Foundation (Grant No. Z220008).

- [1] R. Ulbricht, E. Hendry, J. Shan, T. Heinz, and M. Bonn, Carrier dynamics in semiconductors studied with time-resolved terahertz spectroscopy, *Rev. Mod. Phys.* **83**, 543 (2011).
- [2] X. Yang, X. Zhao, K. Yang, Y. Liu, Y. Liu, W. Fu, and Y. Luo, Biomedical applications of terahertz spectroscopy and imaging, *Trends Biotechnol.* **34**, 810 (2016).
- [3] R. Stantchev, X. Yu, T. Blu, and E. Pickwell-MacPherson, Real-time terahertz imaging with a single-pixel detector, *Nat. Commun.* **11**, 2535 (2020).
- [4] K. Cooper, R. Dengler, G. Chattopadhyay, E. Schlecht, J. Gill, A. Skalare, I. Mehdi, and P. Siegel, A high-resolution imaging radar at 580 GHz, *IEEE Microw. Wirel. Compon. Lett.* **18**, 64 (2008).
- [5] K. Cooper, R. Dengler, N. Llombart, T. Bryllert, G. Chattopadhyay, E. Schlecht, J. Gill, C. Lee, A. Skalare, I. Mehdi, *et al.*, Penetrating 3D imaging at 4- and 25-m range using a submillimeter-wave radar, *IEEE Trans. Microw. Theory Tech.* **56**, 2771 (2008).

- [6] A. Danylov, T. Goyette, J. Waldman, M. Coulombe, A. Gatesman, R. Giles, X. Qian, N. Chandrayan, S. Vangala, K. Termko, *et al.*, Terahertz inverse synthetic aperture radar (ISAR) imaging with a quantum cascade laser transmitter, [Opt. Express](#) **18**, 16264 (2010).
- [7] R. Köhler, A. Tredicucci, F. Beltram, H. Beere, E. Linfield, A. Davies, D. Ritchie, R. Iotti, and F. Rossi, Terahertz semiconductor-heterostructure laser, [Nature](#) **417**, 156 (2002).
- [8] L. Ozyuzer, A. Koshelev, C. Kurter, N. Gopalsami, Q. Li, M. Tachiki, K. Kadokawa, T. Yamamoto, H. Minami, H. Yamaguchi, *et al.*, Emission of coherent THz radiation from superconductors, [Science](#) **318**, 1291 (2007).
- [9] S. Suzuki, M. Shiraishi, H. Shibayama, and M. Asada, High-power operation of terahertz oscillators with resonant tunneling diodes using impedance-matched antennas and array configuration, [IEEE J. Sel. Top. Quantum Electron.](#) **19**, 8500108 (2012).
- [10] W. Liu, L. Liang, Q. Jia, L. Wang, and Y. Lu, Multi-color terahertz frequency mixer using multibunching of free-electron beams, [Phys. Rev. Appl.](#) **10**, 034031 (2018).
- [11] H. Hashiba, V. Antonov, L. Kulik, A. Tzalenchuk, P. Kleinschmid, S. Giblin, and S. Komiyama, Isolated quantum dot in application to terahertz photon counting, [Phys. Rev. B](#) **73**, 081310 (2006).
- [12] R. Shaikhaidarov, V. N. Antonov, A. Casey, A. Kalaboukhov, S. Kubatkin, Y. Harada, K. Onomitsu, A. Tzalenchuk, and A. Sobolev, Detection of coherent terahertz radiation from a high-temperature superconductor Josephson junction by a semiconductor quantum-dot detector, [Phys. Rev. Appl.](#) **5**, 024010 (2016).
- [13] P. Echternach, B. Pepper, T. Reck, and C. Bradford, Single photon detection of 1.5 THz radiation with the quantum capacitance detector, [Nat. Astron.](#) **2**, 90 (2018).
- [14] N. Wang, S. Cakmakyapan, Y. Lin, H. Javadi, and M. Jarrahi, Room-temperature heterodyne terahertz detection with quantum-level sensitivity, [Nat. Astron.](#) **3**, 977 (2019).
- [15] S. Lloyd, Enhanced sensitivity of photodetection via quantum illumination, [Science](#) **321**, 1463 (2008).
- [16] S. Tan, B. Erkmen, V. Giovannetti, S. Guha, S. Lloyd, L. Maccone, S. Pirandola, and J. Shapiro, Quantum illumination with Gaussian states, [Phys. Rev. Lett.](#) **101**, 253601 (2008).
- [17] Q. Zhuang, Z. Zhang, and J. Shapiro, Optimum mixed-state discrimination for noisy entanglement-enhanced sensing, [Phys. Rev. Lett.](#) **118**, 040801 (2017).
- [18] H. Yang, N. Samantaray, and J. Jeffers, Quantum illumination with multiplexed photodetection, [Phys. Rev. Appl.](#) **18**, 034021 (2022).
- [19] S. Barzanjeh, S. Guha, C. Weedbrook, D. Vitali, J. Shapiro, and S. Pirandola, Microwave quantum illumination, [Phys. Rev. Lett.](#) **114**, 080503 (2015).
- [20] R. Nair and M. Gu, Fundamental limits of quantum illumination, [Optica](#) **7**, 771 (2020).
- [21] E. Lopaeva, I. Berchera, I. Degiovanni, S. Olivares, G. Brida, and M. Genovese, Experimental realization of quantum illumination, [Phys. Rev. Lett.](#) **110**, 153603 (2013).
- [22] F. Xu, X. Zhang, L. Xu, T. Jiang, M. Yung, and L. Zhang, Experimental quantum target detection approaching the fundamental Helstrom limit, [Phys. Rev. Lett.](#) **127**, 040504 (2021).
- [23] G. Qian, X. Xu, S. Zhu, C. Xu, F. Gao, V. Yakovlev, X. Liu, S. Zhu, and D. Wang, Quantum induced coherence light detection and ranging, [Phys. Rev. Lett.](#) **131**, 033603 (2023).
- [24] J. M. J. Madey, Stimulated emission of bremsstrahlung in a periodic magnetic field, [J. Appl. Phys.](#) **42**, 1906 (1971).
- [25] L. Zhang, Z. Li, D. Liu, C. Wu, H. Xu, and Z. Li, Entangled x-ray photon pair generation by free-electron lasers, [Phys. Rev. Lett.](#) **131**, 073601 (2023).
- [26] V. Borisov, E. Matushevsky, N. Morozov, E. Syresin, O. Grimm, M. Yurkov, and J. R. Germany, in *Proceedings of EPAC 2006* (The European Physical Society Accelerator Group (EPS-AG), Edinburgh, 2006), p. 3595.
- [27] C. W. Helstrom, *Quantum Detection and Estimation Theory* (Academic Press, New York, 1976).
- [28] S. J. Russell and P. Norvig, *Artificial Intelligence: A Modern Approach* (Pearson, London, 2015), 3rd ed.
- [29] C. Weedbrook, S. Pirandola, R. García-Patrón, N. Cerf, T. Ralph, J. Shapiro, and S. Lloyd, Gaussian quantum information, [Rev. Mod. Phys.](#) **84**, 621 (2012).
- [30] V. I. Ritus, Quantum effects of the interaction of elementary particles with an intense electromagnetic field, [J. Sov. Laser Res.](#) **6**, 497 (1985).
- [31] K.-J. Kim, Z. Huang, and R. Lindberg, *Synchrotron Radiation and Free-Electron Lasers: Principles of Coherent X-Ray Generation* (Cambridge University Press, Cambridge, 2017).